 doi:10.20944/preprints202207.0129.v1

Article

Spectroscopic and Voltammetric Study of Recycled and Cooper-Manganese-Doped Electrode Materials

S. Rada[1, 2], M. Unguresan[1], J. Zhang[3] and E. Culea[1]

[1.] Physics and Chemistry Department, Technical University of Cluj-Napoca, 400020, Romania
[2.] National Institute for Research and Development of Isotopic and Molecular Technologies, 400293, Cluj-Napoca, Romania
[3]Institute of High Energy Physics, Chinese Academy of Sciences, Beijing, 100049, People's Republic of China
* Correspondence: Authors: simona.rada@phys.utcluj.ro; radasimona@yahoo.com (S. Rada)

Abstract

The novelty of this study consists in: i) synthesis and characterization of electrode materials recycled from a spent car battery and doped with MnO_2 and CuO by the analysis of X-ray diffraction (XRD), Infrared (IR) and Electron Paramagnetic Resonance (EPR) data and ii) the investigation of electrochemical properties of prepared materials in view of new applications as electrode materials for battery.

Electron Paramagnetic Resonance (EPR) data indicate that the intensity of the resonance line corresponding to the Cu^{+2} ion was modified with the increase of the dopant content.

The analysis of X-ray Absorption Spectroscopy (XAS) data indicates that by increasing the dopant content there is a process of ordering the oxygen atoms around the lead similar to the PbO_2 theoretical model. The electrochemical performances of the recycled and manganese-copper-doped materials are optimized for applications as new anodic electrode for the car battery.

Keywords: recycled electrode; spent battery; spectroscopic method; cyclic voltammetry

1. Introduction

The most efficient strategies for the electricity energy storage remain the Li/Na-ion batteries and lead acid batteries [1-4]. Among different batteries, lead acid batteries have the following advantages: low price, stability, safety, reliability and convenient maintenance [5].

Today the car battery consists of a lead grid on which a thin layer of active matter is kneaded. The extension of the life of the car battery depends on the quality of the electrodes, namely the composition of the grill and the paste applied on it. The lead grid is made of lead plates that are alloyed with other metals. The lead grid in the so-called unformed state is coated with a lead oxide paste – Pb_3O_4 and/or PbO litharge. The paste consisting of oxides of lead, sulfuric acid and water is applied to the grill. Also expanded materials made of different sulfur powders are added to this paste to make the negative plates. Therefore, the composition of

 doi:10.20944/preprints202207.0129.v1

the electrode may be different in car batteries depending on the oxides used in the paste or the lead content in the grill.

Lead is the main raw material in the fabrication of automotive batteries and cannot be replaced with other material. Nowadays, lead recovery from spent batteries is realized by the pyrometallurgical route. Pyrometallurgy comprises over 90% of the recovery technology and is the smelting process used for recycling of lead acid batteries [6]. The pyrometallurgical technology is composed of four stages: i) separation of components from batteries (plastic, electrolyte and lead plates - all components of battery are reclaimed by further treatments); ii) lead reduction in rotary furnance; iii) separation of metallic lead from slag; iv) refining of recycled lead [7]. The main disadvantage of this route is that may cause environmental problems, such as the emissions of sulphur oxides (obtained by decomposition of lead sulfate at over 1000 ^{o}C) and lead into the atmosphere at high temeprature. Lead industry was made numerous contributions to reduce environmental pollution because the pyrometallurgical technology remains the main method for the recycling of spent lead acid batteries [8, 9]. In order to reduce the processing temperature and the production costs, leaching behaviours were incorporated to remove sulphur before smelting process.

The leaching-electrowinning process was the first proposed method to replace the pyrometallurgical tehnology. Electrowinning process can be divised into two stages: i) solid state electrolysis where $PbSO_4$ and PbO_2 are decomposed into PbO and ii) leaching followed by electrowinning process (based on acid or alkaline leaching agents) when the produced PbO is reduced into metallic lead on the cathode.

In the hydrometallurgy technique lead sulphate is converted into lead carbonate, hydroxide and hydroxyl-carbonate by the dissolvation at low temperature [10 - 13]. The basic problems during hydro-electrometalurgical treatments are the low solubility of lead compounds in solvents and inefficient desulphurization in the aquesous solution.

The leaching-electrowinning process proposed by Andrews [14] uses the dilute NaCl and HCl solutions for spent lead paste. After separation, the $PbCl_2$ solution is purified by adding lead powder (the impurities of metal ions are reduced by lead powder to yield metallic substance) and then, it is electrolyzed to yield metallic lead on the cathode. The remaining acid is neutralized with lime and Na_2SO_4 is used for producing gypsum. In this PLACID process the energy consumption is significantly high and the chloride corrosion causes high maintenance of the equipment.

In brief, almost all components of lead acid battery can be completely recycled and reused by the implementation of low energy input processes [10]. The PLACID process integrated with a pyrometallurgical treatment can be a feasible route for spent lead acid battery recycling. Hydrometallurgy combined with electrochemistry technique can be assigned as eco-friedly process but they are in the incipient stage for the industrial applications [9].

 doi:10.20944/preprints202207.0129.v1

The main problem in the recycling of lead acid battery consists in the introduction of new advanced technologies coexisting with traditional technology. Recently, the melt quenching method was described to inspire the recycling of lead from the spent plates of the lead acid battery by eco-inovative method with low energy and cost consumption [15]. The electrochemical performance of the recycled materials can be improved by the doping with metallic oxides, such as manganese ions [16].

Lead is hard to recycle when is present in lower amounts in electrodes of battery. The purpose of our research was to analyze the structure and applications of the new materials obtained from high sulphatized plates of the spent lead acid battery which has a low amount of lead in plates in view of new applications as electrode for car battery.

In this sense, a new vitreous system recycled from the spent active mass of the used car battery with a high sulphatated degree and doped with CuO and MnO_2 was prepared by melt quenching method in the view of the obtaining of answers related to the quality of the electrodes, the extension of life of the battery and the recycling capacity of the used active mass. The prepared materials will be tested as new electrodes for the car batteries.

2. Experimental procedure

The recycled vitreous systems doped with CuO and MnO_2 in the $xCuO{\cdot}5MnO_2{\cdot}(95\text{-}x)[4PbO_2{\cdot}Pb]$ composition where x = 0, 3, 5, 8, 10, 15, 20, 25, 30, 40 and 50 mol% CuO were prepared by an eco-innovative, less polluting and low energy cost technology, namely melt queching method which was recently published and described by some authors of this paper [7, 8]. As the starting materials are used the anode and the cathode from a spent car battery, laboratory reagents: MnO_2 and CuO powders of over 95 % purity. Mixtures of substances in stoichiometric proportions were placed in a crucible and then kept for 10 minutes in an electric furnance seted at temperature of 900 ^{o}C.

The samples were broken and powdered in agate mortar. The powders of the samples were investigated by the analysis of X-ray diffraction (XRD), Fourier transform infrared (FTIR), electron paramagnetic resonance (EPR) and X-ray absorption (XAS) spectroscopy which were presented in the Refs. [17 - 21].

Experimental X-ray absorption spectroscopy measurements using synchrotron radiation facilities for recycled vitroceramic systems were performed at the Institute of High Energy Physics, Beijing. X-ray Absorption Fine Structure (XAFS) measurements were performed in the energy range of incident radiation between 12,800 and 13,700 eV corresponding to the L3 lead absorption edge by the high energy resolution fluorescence detection. High-energy resolution fluorescence-detected (HERFD) X-ray Absorption Spectyrocopy (XAS) investigates unoccupied states with a spectral resolution higher than regular XAS. HERFD is a powerful new tool for the structure determinations.

 doi:10.20944/preprints202207.0129.v1

For the measurements of cyclic voltammetry, the electrode materials obtained in the form of discs were used as working electrode, the platinum electrode was used as a counter electrode, the calomel electrode as the reference electrode, and the sulfuric acid solution of 38% concentration was used as the electrolyte solution [15 - 19]. In cyclic voltammetry measurements we considered an electrochemical cell made up of three electrodes: the working electrode - it was the material recycled and doped with manganese dioxide and copper oxide, the reference electrode - calomel electrode $Hg/Hg_2Cl_2/KCl$ and a counter electrode - platinum electrode. A sulfuric acid solution of 38% concentration was used to simulate a car battery. Cyclic voltammetry was recorded in the potential range between -1 to 2V at a scan rate of 50 mV/s.

3. Results and discussion

3.1. X-ray diffraction analysis (XRD)

X-ray diffractograms of the recycled system in the composition $xCuO{\cdot}5MnO_2{\cdot}(95\text{-}x)[4PbO_2{\cdot}Pb]$ where x = 0 - 50 mol % CuO synthesized at 900 ^oC were shown in Figure 1. For the host matrix XRD patterns show a vitroceramic structure with five crystalline phases: Pb_2SO_5 (PDF card no. 00-076-1579), $Pb_3O_2SO_4$ (PDF card no. 01-078-0530), PbO_2 (PDF card no. 00-052-0752), Pb_2O_3 (PDF card no. 00-036-0725) and metallic Pb (PDF card no. 03-065-2873). The Pb_2SO_5 ($\equiv PbO{\cdot}PbSO_4$) crystalline phase with monoclinic structure, $Pb_3O_2SO_4$ ($\equiv 2PbO{\cdot}PbSO_4$) crystalline phase with monoclinic structure, Pb_2O_3 ($\equiv PbO{\cdot}PbO_2$) crystalline phase with monoclinic structure, PbO_2 crystalline phase with orthorhombic structure and metallic lead with cubic structure were evidenced in XRD data. By the adding of CuO content up to 8 mol% CuO, the $Pb_3O_2SO_4$ crystalline phase disappears abruptly, the intensity of the diffraction peak situated at about 26.66^o (attributed to the main peak of 100% intensity of the Pb_2SO_5 crystalline phase) decreases and the content of the metalic Pb and PbO_2 crystalline phases were increased. Adding of higher CuO levels in the host matrix produces decreases the amount of Pb_2O_3 and Pb_2SO_5 crystalline phases. For the samples with x = 30 and 50 mol% CuO the decrease of intensity of the diffraction peak centered at about 30.02^o indicate a smaller PbO_2 content in the network structure than at their analogues. For the sample with x = 40 mol% CuO the diffraction peak characteristic to the $Pb_3O_2SO_4$ crystaline phase dissapeared, the amount of Pb_2SO_5 crystaline phase attains minimum value and the content of PbO_2 crystalline phase was increased.

The diffraction peaks centered at about 26.66 and 30.02^o have almost similarly intensity for the sample with x = 30 mol% CuO. This evolution shows

Analysis of these results indicates that the adding of CuO content in the manganese-lead-lead dioxide network produces the partial desulphatization of recycled materials by the descomposition of $Pb_3O_2SO_4$ crystalline phase at 900 ^oC. The described method is an eco-innovative process due to i) the short time of

 doi:10.20944/preprints202207.0129.v1

synthesis at 900°C only ten minutes; ii) the synthesis temperature is below decomposition of lead sulphate (over 1100°C); iii) the adding of 40 mol% CuO produces the decrease of sulphatatized crystalline phases.

3.2. Structural investigation by InfraRed spectroscopy (IR)

The FTIR absorption spectra of the vitreous system with the composition $xCuO \cdot 5MnO_2 \cdot (95-x)[4PbO_2 \cdot Pb]$ where x=0-50 mol% CuO are shown in Figure 2 and the assignment of the IR bands is illustrated in Table 1.

IR data indicate some important structural modifications by increasing the CuO content in the vitroceramic matrix, which can be systematized as follows:

i) IR bands with smaller intensity situated between 350 and 550 cm^{-1} are associated with the contributions provenied from the bending vibrations of the O-Pb-P and Pb-O-Pb angles from $[PbO_4]$ structural units [22, 23] overlapped with the stretching vibrations of the Cu-O and Mn-O bonds [24, 25]. An increasing trend in the intensity of the IR bands can be evidenced by increasing of CuO contents up to 15 mol% CuO after that a decreasing tendency is evidenced by the addition of higher dopant contents up to x = 50 mol% CuO. This structural evolution can be explained considering the increase of the degree of polymerization of Pb-O-Cu and Pb-O-Mn linkages by the doping up to 15 mol% CuO.

ii) The second region of IR bands of intermediate intensity located between 550 and 650 cm^{-1} is derived from the overlaps of stretching vibrations of the metal - O bonds and the stretching vibrations of S - O bonds in the sulphate units (620 – 640 cm^{-1}) [26]. By doping with copper (II) oxide, the IR bands in this region become intensely up to 15 mol% CuO and then were decreased for higher dopant levels.

iii) The IR bands situated between 650 and 1000 cm^{-1} are consisted of the following contributions: the stretching vibrations of Pb-O bonds from $[PbO_4]$ and $[PbO_6]$ structural units (IR bands centered at about 680 and 875 cm^{-1}) and the stretching vibrations of the Cu-O bonds in the $[CuO_n]$ structural units with n = 4 and 6 (IR bands situated at 620 and 860 cm^{-1}, respectively) [23]. The intensities of these bands reach high values by the doping with CuO content up to 15 mol%.

iv) The last region of high-intensity IR bands located between 1000 and 1200 cm^{-1} is associated with the stretching vibrations of the S = O bonds from sulphate units (1075 cm^{-1}) and asymmetric stretching vibrations of the sulphate units (1120 cm^{-1}) ovellaped with Pb - O stretching vibrations from $[PbO_n]$ structural units with n = 3 and 4. The intensity of the band located at about 1075 cm^{-1} increases up to 15 mol% CuO after that a drastic decrease was evidenced for higher CuO contents. The broadening of the IR band centered at about 1120 cm^{-1} becomes more formed and intense for the samples containing up to 15 mol% CuO. By adding of higher CuO contents, the feature of this band decreases and shifts towards lower wavenumbers.

Preprints (www.preprints.org) | NOT PEER-REVIEWED | Posted: 8 July 2022 doi:10.20944/preprints202207.0129.v1

These evolutions suggest a sudden decrease in the amount of sulphate units in the vitroceramic structure by the doping with higher CuO levels, in acord with XRD data. For the samples with x= 40 and 50 mol% CuO the amount of sulphated units reachs small values.

The IR bands in the region between 400 and 600 cm^{-1} are due to vibrations of the Pb^{+2} ions, then the two weak IR bands located at 695 and 870 cm^{-1} report the presence of PbO nanoparticles [24]. This evolution indicates that the content of the crystalline phase Pb_2O_3 reaches a maximum value for the sample with x = 15 mol% CuO. For higher concentrations of dopant there is a conversion of the crystalline phases Pb_2SO_5 and Pb_2O_3 from vitroceramic to the predominant crystalline phase with PbO_2 nanoparticles. For the samples with $x \leq 15$ mol% CuO, the excess oxygen is accumulated in the vitroceramic by the formation of structural units $[PbO_n]$ with n = 3, 4 and 6 while at higher dopant levels are predominantly n = 3 and 4. To verify this transformation from vitroceramic formed from the predominant phase with PbO nanoparticles into the predominant crystalline phase with PbO_2 nanoparticles for higher CuO concentrations above x > 15 mol%, in the section with structural investigations by X-ray absorption spectroscopy with synchrotronic radiation, PbO_2 will be used as a theoretical model in the simulation by EXAFS.

3.3. Structural investigation by spectroscopy of Electron Paramagnetic Resonance (ESR)

The local structure and geometry of the two paramagnetic ions, namely manganese and copper ions are investigated by EPR spectroscopy. The EPR spectra of the recycled system in the $xCuO \cdot 5MnO_2 \cdot (95-x)[4PbO_2 \cdot Pb]$ composition with x = 0 - 50 mol% CuO measured at room temperature are shown in Figure 3. The presence of three resonance lines located at g ~ 2, 4.3 and 8 (between 8 and 9) are observed in the undoped sample. The resonance signal located at g ~ 2 is assigned to the Mn^{+2} ions located in sites with distorted octahedral geometry [25]. The resonance line centered at about g ~ 4.3 corresponds to the rhombic symmetry of Mn^{+2} ions. While the resonance signal located at g ~ 8 is due to the Mn^{+3} ions (at the magnetic field intensity, H~800G in the X band) [26]. The structural and magnetic studies of the manganese-doped glasses reveal that both Mn^{+2} and Mn^{+3} ions exist in the framework of these samples [27 -29].

The analysis of EPR data for $CuO-MnO_2$ doped vitroceramics indicates changes of the resonance lines with the increase of CuO content. By doping with CuO concentration, the resonance line located at g ~ 2 corresponds to the Cu^{+2} ions located at sites with distorted octahedral symmetry which was overllaped over resonance signal at g ~ 2 attributed to the Mn^{+2} ions. The resonance line at g ~ 4.3 appears only for samples with $x \leq 5$ mol% CuO. The intensity of the resonance line centered at g ~ 8 increases in intensity up to $x \leq 8$ mol% CuO, after that it decreases for the sample with x = 10 mol% CuO, and for the samples with $15 \geq x \leq 25$ mol% CuO a parallel component appears in the hyperfine structure and at higher CuO contents, $x \geq 30$

Preprints (www.preprints.org) | NOT PEER-REVIEWED | Posted: 8 July 2022 doi:10.20944/preprints202207.0129.v1

mol% CuO the intensity was increased again. The appearance of the hyperfine structure for samples with 15 ≥ x ≤ 25 mol % CuO indicates a process of ordering of the oxygen atoms around Mn^{+3} ions.

The resonance line located at g ~ 2 is dependent on the CuO content of the glass ceramic structure. For samples with x ≤ 20 mol% CuO appears a hyperfine structure with a well resolved parallel component attributed to Cu^{+2} ions. By increasing of the dopant level to x = 25 and 30 mol % CuO, a large signal appears due to the clustered Cu^{+2} and Mn^{+2} ions. For higher dopant levels up to x = 40 mol% CuO, the appearance of a weakly resolved hyperfine structure superimposed with a broader resonance line attributed to the clustered Cu^{+2} ions can be highlighted. The presence of hyperfine structure at high dopant contents indicates the conversion of $Cu^{+2} \rightarrow Cu^{+1}$ ions by the doping process. Therefore, through the addition of high dopant contents, a process for the conversion of $Cu^{+2} \rightarrow Cu^{+1}$ and $Mn^{+2} \rightarrow Mn^{+3}$ ions takes place (the latter is performed during the synthesis when the melting is abruptly cooled down).

3.4. X-ray absorption spectroscopy (XAS) measurements with synchrotronic radiation

XANES spectra for the L3 edge of lead in the energy range 12,800 and 13,700 eV (XANES representation is only indicated in this field for clarity) for recycled vitreous systems in the composition $xCuO{\cdot}5MnO_2{\cdot}(95\text{-}x)[4PbO_2{\cdot}Pb]$ where x=0-50 mol% CuO are shown in Figures 5 and 6.

In the XANES spectra, for a better distinction of the energy variation, the spectra of the first derivative of the absorption coefficient for the L3 edge of the lead are represented in Figure 5. A first observation regarding the XANES spectra is that the energy position of the first main absorption band was modified with increasing CuO concentration in the host matrix which indicates variations in the lead valence.

The literature data indicate for PbO_2 in the XANES spectra, the absorption edge centered at 13035.7 eV and other three main bands located at 13046.1, 13,055 and 13065eV. For the yellow PbO the bands for the L3 edge of the lead atom are located at 13038, 13049.4 and 13061.1eV, while for its allotropic red PbO the bands are centered at 13037, 13047.8 and 13060eV [30 - 32].

XANES data analysis indicates that the position of the absorption edge is similar to that corresponding to the characteristic features of the PbO_2 powder. The position of the bands at 13037.62 and 13047.5 eV (for the sample with x = 0 mol% CuO) are characteristic features similar to that of the red PbO powder. As a result, lead is found in the oxidation state +4 and +2 in the studied system.

Detailed information about the local environment of the studied system can be obtained from the EXAFS spectra. EXAFS (Extended X-ray Absorption Fine Structure) provides information about the local coordination structure of the given atom, including the coordination number and distances between neighboring atoms. In this sense, for the simulation of EXAFS with the Artemis program, a PbO_2 theoretical model will be used for all the recycled samples. The radial distribution functions of the lead atom for the

 doi:10.20944/preprints202207.0129.v1

recycled vitroceramic systems having the $xCuO \cdot 5MnO_2 \cdot (95\text{-}x)[4PbO_2 \cdot Pb]$ composition where x = 0 - 50 mol% CuO are shown in Figure 7.

The analysis of the Fourier transform of the EXAFS oscillations at the L3 edge of the lead atom for the studied system shows for all the samples three principal coordination spheres that are detected around the lead atom: short Pb-O distance, long Pb-O distance, Pb-Pb and other longer Pb-metal distances. The first EXAFS oscillation located between 1.2 and 2.4 Å corresponds to the interatomic Pb-O distance from its immediate vicinity in the first coordination sphere. Changes in the intensity of this oscillation indicate that the first sphere of coordination is affected by the increase of CuO content in the host matrix. Thus, the changes in the intensity of the Fourier transform of the first EXAFS oscillation by increasing the dopant level show the modification of the average oxidation number of the lead atom.

Table 2 presents the parameters that describe the local structure for the investigated glass system: the number of atoms in the first coordination sphere, N, the interatomic Pb-O distances, the Debye Waller thermal disorder parameter, σ^2 and the bond energy, E_o. The parameter of Debye Waller thermal disorder is less than 0.002, which indicates that the theoretical model used, respectively PbO_2, was well chosen for the studied samples.

The energy peak position of the first derivative of the absorption coefficient depending on energy and the peak situated at about 13051.8eV has maximum value (Figure 6, Table 2). The thermal disorder parameter Debye Waller attains maximum value for the host matrix (Table 3).

The average Pb-O distance in the tetravalent compound PbO_2 is 2.16 Å when the lead atom is hexacoordinated. In the case of divalent lead, the interatomic distance Pb-O is 2.66 Å in $PbTiO_3$ with coordination number 8. According to the data in Table 3 we assume that the lead in all the studied samples can be tetracoordinated and the distance Pb-O in the first coordination sphere is higher than 2.16 Å and slightly smaller than 2.66 Å. The wide difference from 2.16 Å (between 2.26 and 2.30 Å) suggests the distortions of the coordination geometry are produced by the substitution of the sites occupied by divalent lead ions.

The length of the Pb-O bond in the first coordination sphere has a minimum value for the sample with x = 50 mol% CuO, followed by that with x = 40 mol% CuO. This evolution suggests that through doping with high dopant contents, a process of ordering lead-based vitroceramics takes place with a trend towards a structure similar to that of lead dioxide.

3.5. Testing the electrochemical performance of the electrode materials by measurements of cyclic voltammetry

Cyclic voltammetry measurements for recycled and doped materials, with copper oxide and manganese dioxide, provide significant information regarding the mechanism of reduction and oxidation of

Preprints (www.preprints.org) | NOT PEER-REVIEWED | Posted: 8 July 2022 doi:10.20944/preprints202207.0129.v1

the different chemical species present in the tested electrode materials in the electrolyte solutions. Cyclic voltammograms of recycled materials in the $xCuO{\cdot}5MnO_2{\cdot}(95\text{-}x)[4PbO_2{\cdot}Pb]$ composition where x = 0 - 50 mol% CuO used as working electrode in an electrochemical cell which uses as an electrolyte 38% sulfuric acid solution are shown in Figure 8 (after scanning a cycle) and Figure 10 (after scanning three cycles). From Figure 8 it is noted that the highest current densities are obtained in the case of the samples with x = 3 and 8 mo% CuO.

For the sample with x= 40 mol% CuO the broadening of cyclic voltammogram and the oxidation and reduction waves becomes more formed and intense than for its analogue with x = 3 and 8 mol% CuO (see Figure 9a). In Figure 9b) is represented the cyclic voltammogram of the electrode material with x = 40 mol% CuO with the describing of the redox processes. The sample with x = 40 mol% CuO has the smallest content of sulphatised crystalline phases. The first anodic peak centered at about -0.55 V corresponds to two contributions provided from the $HPbO_2^{-}$/Pb (wave located at -0.54 V) and PbO/Pb (-0.58 V) redox systems. In the region with the positive current density well defined peaks appear centered at about +0.28 V and 0.84 V assigned to the PbO_2/Pb^{+2} and Pb^{+4}/Pb redox processes, respectively. In the cathodic region with negative current density a reduction wave is observed which corresponds to the Pb^0/Pb^{2+} (peak situated at about -0.126V) and $Pb/PbSO_4$ redox systems (-0.356V).

From Figure 10, after a three-cycle scan, a better reversibility of the cyclic voltammogram for the samples with x = 3 and 8 mol% CuO are observed. For the other electrode materials, the voltammogram indicates a high degree of irreversibility, which suggests that the processes are not reversible when the battery is charged.

In conclusion, the recycled and doped sample with x = 3 mol% CuO can be recommended as a new anode electrode for car battery because has the highest current density but the irreversible sulfation during the high rate partial state of charge cycle witll result in the rapid service failure of lead acid battery. The sample with x = 40 mol% CuO reveals a large oxidation, reduction peak area and a higher oxidation/reduction peak current which significantly improves the redox process in the battery. The presence of copper and manganese ions in the composition of the recycled electrode material decreases the passivation phenomenon of the electrode in the region of potential between 0 and 2V and the hydrogen evolution reactions are missing.

4. Conclusions

In this paper, the recyclated vitroceramic systems in the $xCuO{\cdot}5MnO_2{\cdot}(95\text{-}x)[4PbO_2{\cdot}Pb]$ composition where x = 0 – 50 mol% CuO by an eco-innovative technology with low cost and energy, namely melt quenching method was investigatedcharacterized by X-ray diffraction analysis, IR spectroscopy, EPR spectroscopy. Detailed analysis of the vitroceramic structure was performed by X-ray absorption spectroscopy

 doi:10.20944/preprints202207.0129.v1

using the facilities with synchrotronic radiation. As starting materials, the anode electrode was used as a source of lead and the cathode electrode as the source of lead dioxide – taken from a spent car battery. The testing of the electrochemical performance of the prepared samples as new electrodes for the batteries has been demonstrated by cyclic voltammetry measurements.

For the host matrix XRD patterns show a vitroceramic structure with five crystalline phases: Pb_2SO_5 ($\equiv PbO \cdot PbSO_4$) crystalline phase with monoclinic structure, $Pb_3O_2SO_4$ ($\equiv 2PbO \cdot PbSO_4$) crystalline phase with monoclinic structure, Pb_2O_3 ($\equiv PbO \cdot PbO_2$) crystalline phase with monoclinic structure, PbO_2 crystalline phase with orthorhombic structure and metallic lead with cubic structure.

The presence of three resonance lines located at g ~ 2, 4.3 and 8 (between 8 and 9) are observed in the samples. The first and second resonance lines correspond to the rhombic symmetry of Mn^{+2} ions. While the resonance signal located at g ~ 8 is due to the Mn^{+3} ions.

The EXAFS data show that the lead in all the studied samples can be tetracoordinated and the distance Pb-O in the first coordination sphere is higher than 2.16 Å and slightly smaller than 2.66 Å. The wide difference from 2.16 Å (between 2.26 and 2.30 Å) suggests the distortions of the coordination geometry are produced by the substitution of the sites occupied by divalent lead ions.

The conclusions can be summarized as follows: i) the recycling and doping with copper-manganese oxides of the spent battery waste was done at 900^{o}C; ii) a partial desulphatization process of the electrode materials was occurred by doping with CuO contents; iii) the presence of manganese and copper ions in the recycled vitroceramic samples were detailed from the EPR and CV data; iv) the electrode material with a content of x = 40% mole CuO has the smallest content of sulphatized crystalline phases, does not show hydrogen evolution reactions in the sulfuric acid solution and the passivation phenomenon is decreased by increasing the current density in the region of potential between 0 and 2V, which is why we recommend it as an new electrode for the car battery; v) the recycled and optimized materials produced in the melt-quecching method can be used directly by battery manufacturers as electrod.

References

1. W. Tianyi, S. Dawei, S. Devaraj, R. Teofilo, A. Michel, W. Guoxiu, Electrode materials for sodium-ion batteries: considerations on crystal structures and sodium storage mechanisms, Electrochem. Energy Rev. 1 (2018) 200-237.
2. Y. Ding, Z. P. Cano, A. Yu, J. Lu, Z. Chen, Automotive Li-ion batteries: current status and future perspectives, Electrochem. Energy Rev. 2 (2019) 1-28.
3. D. Pavlov, Lead-acid Batteries: Science and Technology, Elsevier Science, 2017.

 doi:10.20944/preprints202207.0129.v1

4. J. Joey, Z. Lei, Z. Jiujun, Lead-acid battery technology: fundamentals, materials and applications, Crc Press, 2015.

5. M. Shi, J. Yuan, L. Dong, D. Zhang, A. Li, J. Zhang, Combining physicochemical model with the equivalent circuit model for performance prediction and optimization of lead-acid batteries, Electrochimica Acta 353 (2020) 136567-136577.

6. Z. Shu, H. Cao, X. Zhang, X. Lin, W. Zheng, G. Cao, Y. Sun, Y. Zhang, Spent lead acid battery recycling in China – A review and sustainable analyses on mass flow of lead, Waste Management 64 (2017) 190-201.

7. L. Li, X. Zhu, D. Yang, L. Gao, J. Liu, R.V. Kumar, J. Yang, Preparation and characterization of nano-structured lead oxide from spent lead acid battery paste, J. Hazard. Mater. 203 (2012) 274-282.

8. M. A. Kreusch, M. J .J. S. Ponte, H. A. Ponte, N. M. S. Kaminari, C. E. B. Marino, V. Mymrin, Technological improvements in automotive battery recycling, Resour. Conserv. Recycl. 52 (2007) 368-380.

9. K. Varshney, P. K. Varshney, K. Gautam, M. Tanwar, M. Chaudhary, Current trends and future perspectives in the recycling of spent lead acid batteries in India, Materials Today Proceedings 26 (2020) 592-602.

10. G. J. May, A. Davidson, B. Monaho, Lead batteries for utility energy storage: A review, J. Energy Storage 15(2018) 145-157.

11. Y. Ma, K. Qiu, Recovery of lead from lead paste in spent lead acid battery by hydrometallurgical desulfurization and vacuum thermal reduction, Waste Management 40 (2015) 151-156.

12. Y. Wenhao, J. Yang, M. Li, H. Yuchen, Sh. Liang, J. Wang, P. Zhang, K. Xiao, H. Hou, H. Jingping, R. V. Kumar, A facile lead acetate conversion process for synthesis of high purity alpha lead oxide derived from spent lead acid batteries, J Chem Technol. Biotechnol. 94 (2019) 88–97.

13. M. Somez, R. Kumar, Leaching of waste battery components, Part I: Lead citrate synthesis from PbO and PbO2, Hydrometallurgy, 95(1-2) (2009) 53-60.

14. D. Andrews, A. Raychaudhuri, C. Frias, Environmentally sound technologies for recycling secondary lead, J. Power Sources 88 (2000) 124–129.

15. S. Rada, M. Unguresan, L. Bolundut, M. Rada, H. Vermesan, M. Pica, E. Culea, Structural and electrochemical investigations of the electrodes obtained by recycling of lead acid batteries. J. Electroanalytical Chemistry 780 (2016) 187-196;

 doi:10.20944/preprints202207.0129.v1

16. S. Rada, D. Cuibus, H. Vermesan, M. Rada, E. Culea, Structural and electrochemical properties of recycled active electrodes from spent lead acid battery and modified with different manganese dioxide contents, Electrochimica Acta 268 (2018) 332-339.

17. S. Rada, M. Unguresan, M. Rada, D. Cuibus, J. Zhang, Pengfei An, R. Suciu, A. Bot, E. Culea, Manganese-lead-lead dioxide glass ceramics as electrode materials, J. Electrochem. Soc. 166 (16) (2019) A3987-A3996

18. M. Rada, A. Popa, S. Rada, A. Bot, E. Culea, Recycled and vanadium-doped materials as negative electrode of the lead acid battery, Journal of Solid State Electrochemistry 23 (2019) 2435–2445

19. S. Rada, M. Unguresan, M. Rada, C. Tudoran, Jiaou Wang, E. Culea, Performance of the recycled and copper-doped materials from spent electrodes by XPS and Voltammetric characteristics, J. Electrochem. Soc. 167 (2020) 090548-090554.

20. L. Pop, S. Rada, P. An, J. Zhang, M. Rada, R. Suciu, E. Culea, Characteristics and local structure of hafnia-silicate-zirconate ceramic nanomixtures, J. Synchrotron Radiation 27 (2020) 970-978

21. A. Dehelean, S. Rada, J. Zhang, Determination of the lead environment in samarium-lead oxide-borate glasses and vitroceramics using XANES and EXAFS studies, Radiation Physics and Chemistry 174 (2020) 1089927-1089938.

22. S. Rada, M. Zagrai, M. Rada, L. Magerusan, A. Popa, R. Suciu, S. Macavei, M. Suciu, Structure, electrochemical characterizations and the role of copper oxide in lead-lead dioxide glasses and vitroceramics, J. Non-Cryst. Solids 491 (2018) 55-63.

23. S. Rada, L. Rus, M. Rada, E. Culea, N. Aldea, S. Stan, R. C. Suciu, A. Bot, Synthesis, structure, optical and electrochemical properties of the lead sulfate-lead dioxide-lead glasses and vitroceramics, Solid State Ionics 274 (2015) 111-118.

24. M. El-Toony, Gh. Eid, H. M. Algarni, T. F. Alhawimal, E. E. Abel-hady, Synthesis and characterization of smart polyvinilester/Pb_2O_3 nanocomposite for gamma radiation shielding, Radiation Physics and Chemistry 168 (2020) 108536-108544.

25. A. Dehelean, A. Popa, S. Rada, R. Suciu, M. Stan, E. Culea, Spectroscopic investigation of new manganese tellurite glasses synthesized by sol-gel method, J. Alloys Compounds 801 (2019) 181-187.

26. S. V. Stefanovsky, O. I. Stefanovsky, I. L. Prusakov, M. I. Kadyko, A. A. Averin, B. S. Nikonov, Specifiation of sulphate ions in sodium alumino (iron) phosphate glasses, J. Non-Cryst. Solids 512 (2019) 81-89.

 doi:10.20944/preprints202207.0129.v1

27. C. H. Chang, D. Svedruz, A. Ozarowski, L. Walker, G. Yeagle, R. D. Britt, A. Angerhofer, N. G. J. Richards, EPR spectroscopic characterization of the managanese center and a free radical in the oxalate decarboxylase reaction: identification of a tyrosil radical during turnover, The J. Biological Chemistry 279(51) (2004) 52840–52849.

28. P. Pascuta, M. Bosca, G. Borodi, E. Culea, Thermal, structural and magnetic properties of zinc phosphate glasses doped with manganese ions, J. Alloys Compounds 509(11) (2011) 4314-4319

29. I. Ardelean, N. Muresan, P. Pascuta, EPR and magnetic susceptibility studies of manganese ions in $70TeO_2 \cdot 25B_2O_3 \cdot 5SrO$ glass matrix, Mater. Chem. Phys. 101(1) (2007) 177-181.

30. J. Rybicki, A. Rybicka, A. Witkowska, G. Bergmanski, A. D. Cicco, M. Minicucci, G. Mancini, The structure of lead-silicate glasses: molecular dynamics and EXAFS studies, J. Phys.: Condens. Matter 13 (2001) 9781-9797.

31. A. Dehelean, S. Rada, J. Zhang, Determination of the lead environment in samarium-lead oxide-borate glasses and vitroceramics using XANES and EXAFS studies, Radiation Physiscs and Chemistry 174 (2020) 108927.

32. S. Contessi, M. C. Dalconi, S. Pollastri, L. Calgaro, C. Meneghini, G. Ferrari, A. Marcomini, G. Artioli, Cement-stabilized contamined soil: Understanding Pb retention with XANES and Raman spectroscopy, Science of the Total Environment 752 (2021) 141826.

33. Y. H. Yu, T. Tyliszczak, A. P. Hitchcock, Pb L3 EXAFS and near-edge studies of lead metal and lead oxides, J. Phys. Chem. Solids 51(5) (1990) 445-451.

Preprints (www.preprints.org) | NOT PEER-REVIEWED | Posted: 8 July 2022 doi:10.20944/preprints202207.0129.v1

Table 1: Wave numbers and the assignment of IR bands for the studied system

Wave no. [cm^{-1}]	**IR band assignment**
360-560	Angle deformation vibrations of the Pb-O-Pb and O-Pb-O angles in the structural units [PbO_4] and the elongation vibrations of the Cu-O bond
465	Angle deformation of Pb-O-Pb and O-Pb-O in [PbO_4] structural units
400-600	Vibration due to metal ion Pb^{+2}
560-740	Angle deformation vibrations Pb-O-Cu and Cu-O-Cu
620	Extension vibrations of the Cu-O bond in the structural units [CuO_4]
650-850	Extension vibrations of the Pb-O bond in the structural units [PbO_n]
860	Extension vibrations of Cu-O bonds in structural units [CuO_6]
875	Extension vibrations of Pb-O bond in structural units[PbO_6]
900-1200	Extension vibrations of Pb-O bond in in structural units[PbO_n]with n=3 and 4
600, 1050, 1150	Vibrations corresponding to sulphate ions

Table 2: The global structure parameters for the lead atom in the first coordination sphere for recycled vitreous systems having the composition$xCuO{\cdot}5MnO_2{\cdot}(95\text{-}x)[4PbO_2{\cdot}Pb]$ where x=0-50 mol% CuO.

Sample investigated	Number of atoms of the first coordination sphere N_1	Distance of interatomic radii Pb-O R_1 $\pm\Delta R_1$ [Å]	Thermal disorder parameter Debye Waller (σ^2)	Binding energy, E_0 [eV]
x = 0	4	2.2936	0.00199	13038.909
x = 3	4	2.2941	0.00164	13036.932
x = 5	4	2.2942	0.00158	13036.932
x = 8	4	2.2959	0.00184	13038.992
x = 10	4	2.3057	0.00192	13038.992

 doi:10.20944/preprints202207.0129.v1

x = 20	4	2.30575	0.00193	13038.992
x = 30	4	2.30576	0.00195	13038.992
x = 40	4	2.2910	0.00102	13039.074
x = 50	4	2.2626	0.00028	13036.19

Figures Caption

Fig. 1: X-ray diffractograms for the recycled system with the $xCuO{\cdot}5MnO_2{\cdot}(95\text{-}x)[4PbO_2{\cdot}Pb]$ composition where x = 0 – 50 mol% CuO.

Fig. 2: IR absorption spectra for the recycled system with the $xCuO{\cdot}5MnO_2{\cdot}(95\text{-}x)[4PbO_2{\cdot}Pb]$ composition where: (a) x = 0 - 15 mol% CuO; (b) x = 15 – 50 mol% CuO.

Fig. 3: EPR spectra of the recycled system having the $xCuO{\cdot}5MnO_2{\cdot}(95\text{-}x)[4PbO_2{\cdot}Pb]$ composition with x = 0-50mol% CuO.

Fig. 4: XANES spectra for the L3 lead edge for systems $xCuO{\cdot}5MnO_2{\cdot}(95\text{-}x)[4PbO_2{\cdot}Pb]$ where x = 0 - 50 mol% CuO in the region between 13000 and 13200 eV with the error bars.

Fig. 5: XANES spectra for the L3 lead edge of studied systems in the $xCuO{\cdot}5MnO_2{\cdot}(95\text{-}x)[4PbO_2{\cdot}Pb]$ composition where x = 0 - 50 mol% CuO in the region between 13040 and 13080eV.

Fig. 6: The first XANES derivative for the L3 lead edge for recycled vitreous systems having the $xCuO{\cdot}5MnO_2{\cdot}(95\text{-}x)[4PbO_2{\cdot}Pb]$ composition where x = 0 - 50 mol% CuO.

Fig. 7: Radial distribution functions of the lead atom for recycled systems having the $xCuO{\cdot}5MnO_2{\cdot}(95\text{-}x)[4PbO_2{\cdot}Pb]$ composition where x = 0 - 50 mol% CuO.

Fig. 8: Cyclic voltammograms for the vitreous system with the $xCuO{\cdot}5MnO_2{\cdot}(95\text{-}x)[4PbO_2{\cdot}Pb]$ composition where x = 0 - 50 mol% CuO, in 38% sulfuric acid electrolyte solution.

Preprints (www.preprints.org) | NOT PEER-REVIEWED | Posted: 8 July 2022 doi:10.20944/preprints202207.0129.v1

Fig. 9: Cyclic voltamograms for the vitreous system in the $xCuO{\cdot}5MnO_2{\cdot}(95\text{-}x)[4PbO_2{\cdot}Pb]$ composition where x = 3, 8 and 40 mol% CuO.

Fig. 10: Cyclic voltammograms for the vitreous system with the composition $xCuO{\cdot}5MnO_2{\cdot}(95\text{-}x)[4PbO_2{\cdot}Pb]$, scanned after three cycles in 38% sulfuric acid electrolyte solution.

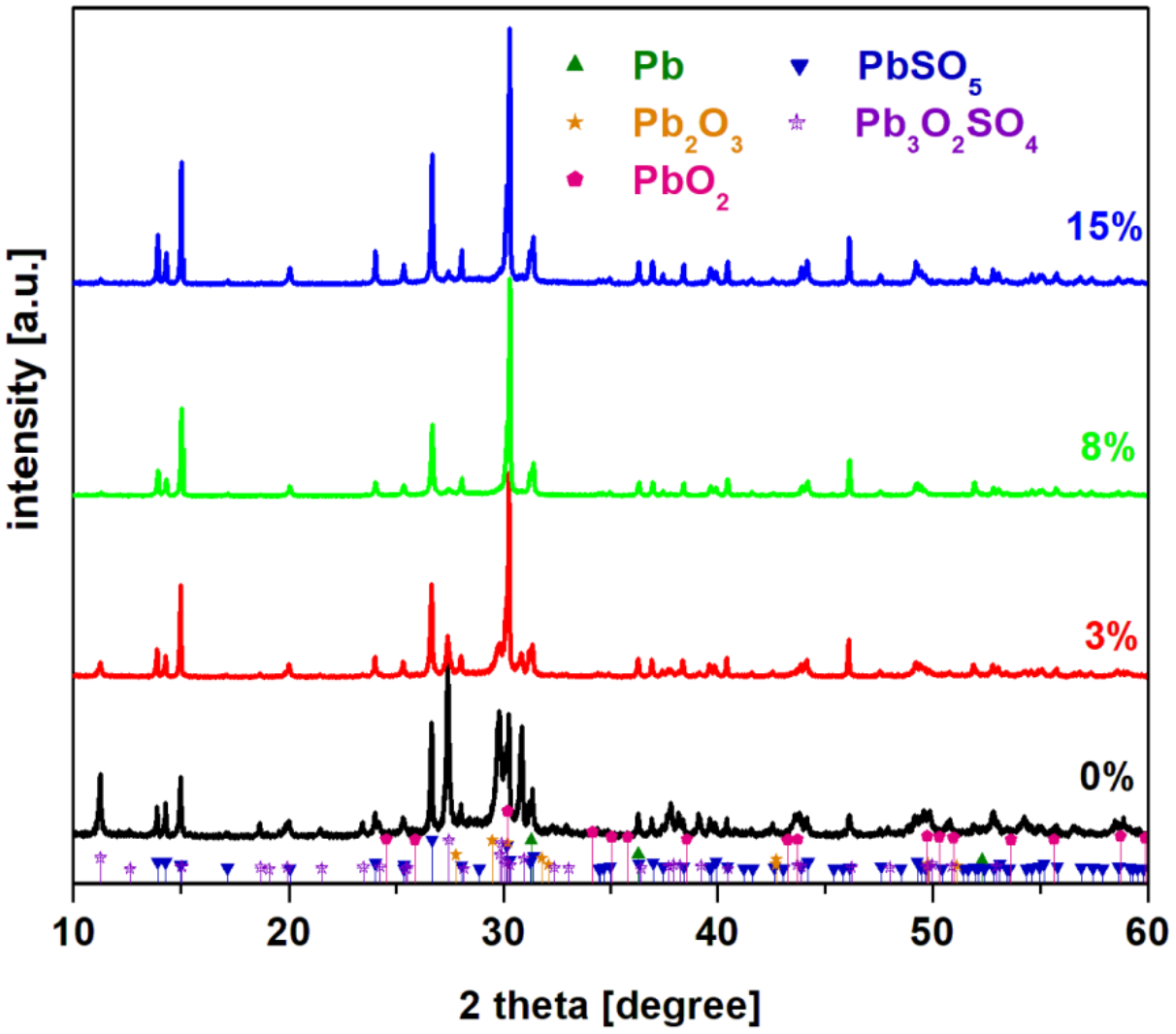

Figure 1a

 doi:10.20944/preprints202207.0129.v1

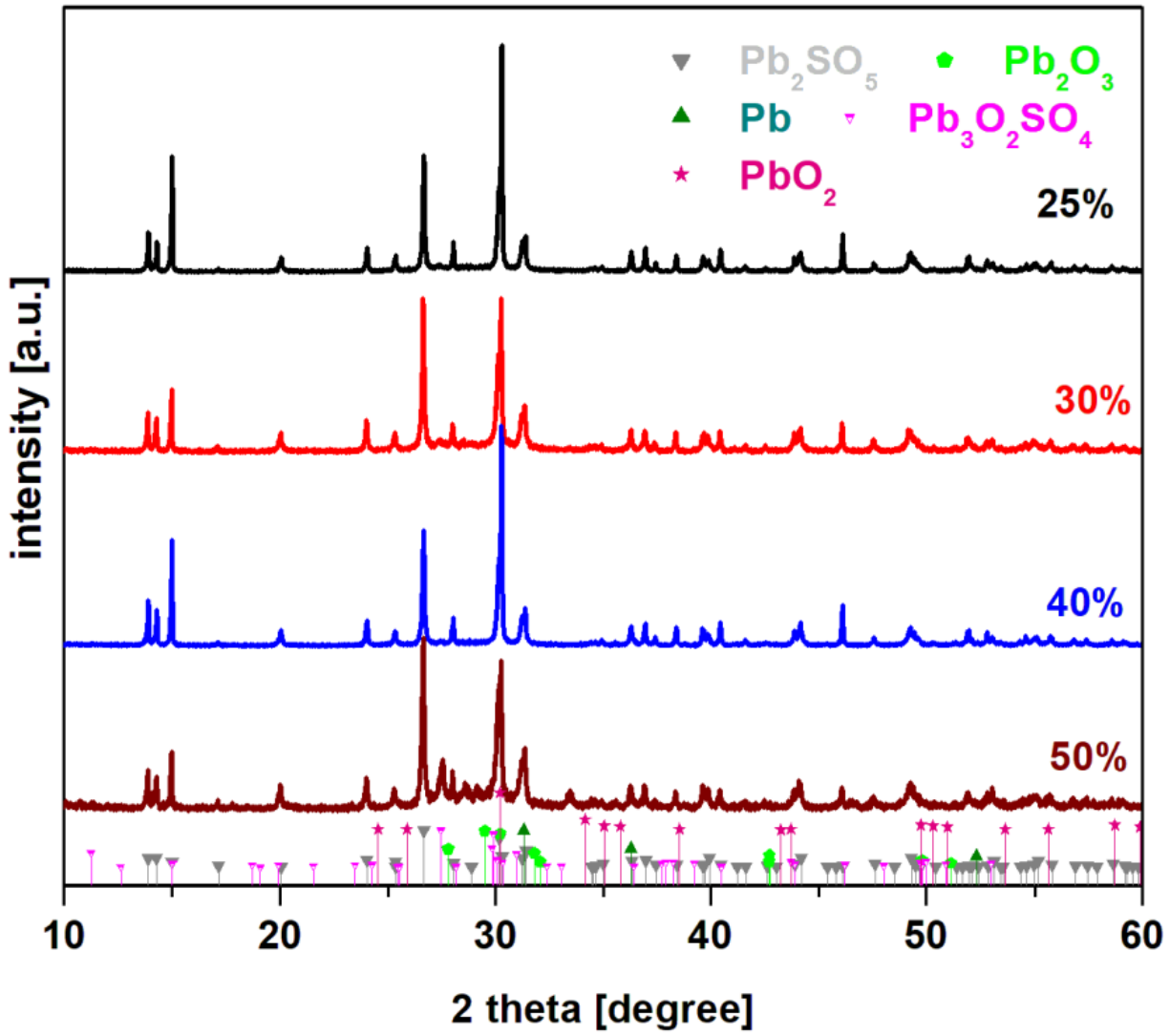

Figure 1b

Preprints (www.preprints.org) | NOT PEER-REVIEWED | Posted: 8 July 2022 doi:10.20944/preprints202207.0129.v1

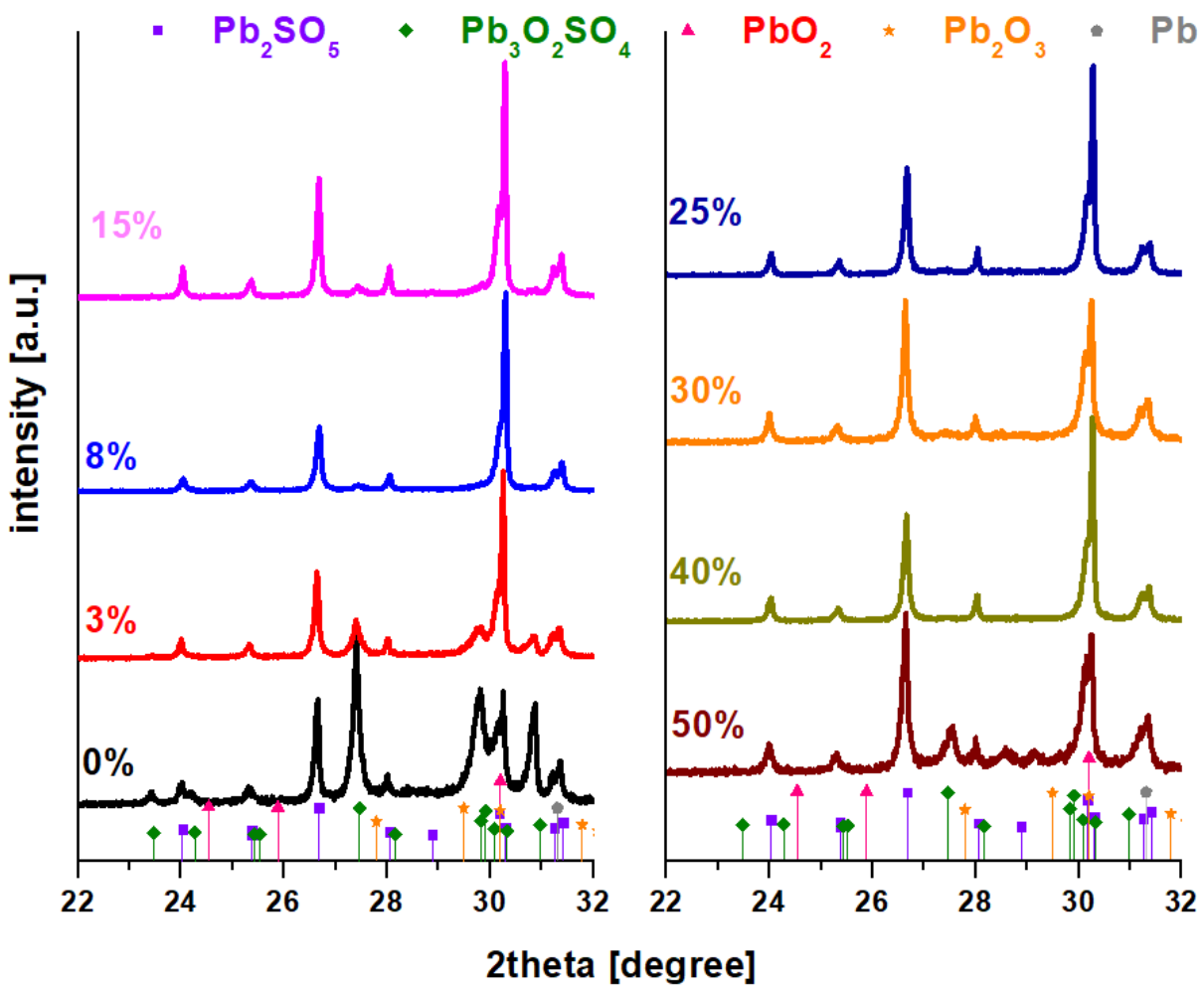

Figure 1c

 doi:10.20944/preprints202207.0129.v1

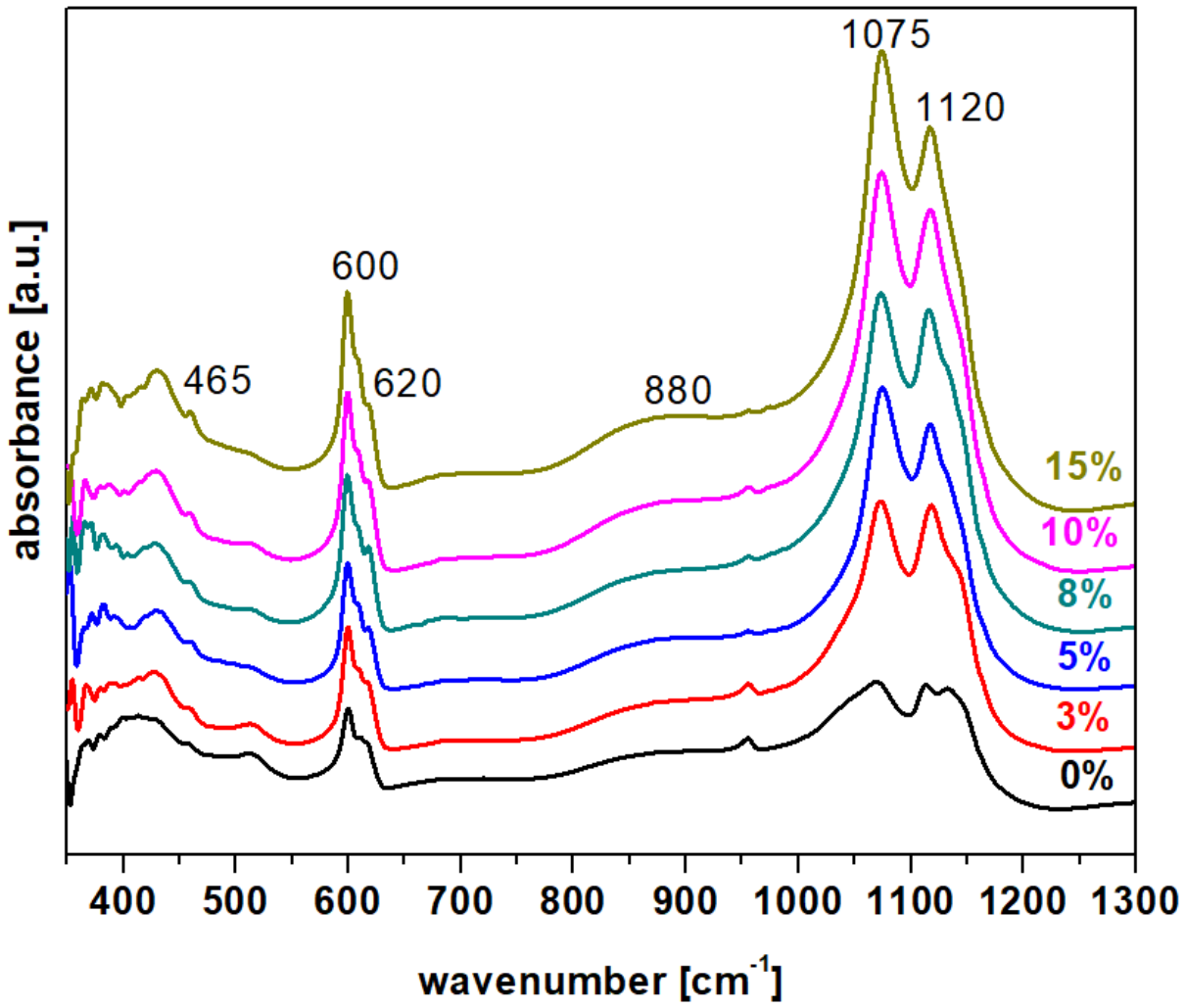

Figure 2a

Preprints (www.preprints.org) | NOT PEER-REVIEWED | Posted: 8 July 2022 doi:10.20944/preprints202207.0129.v1

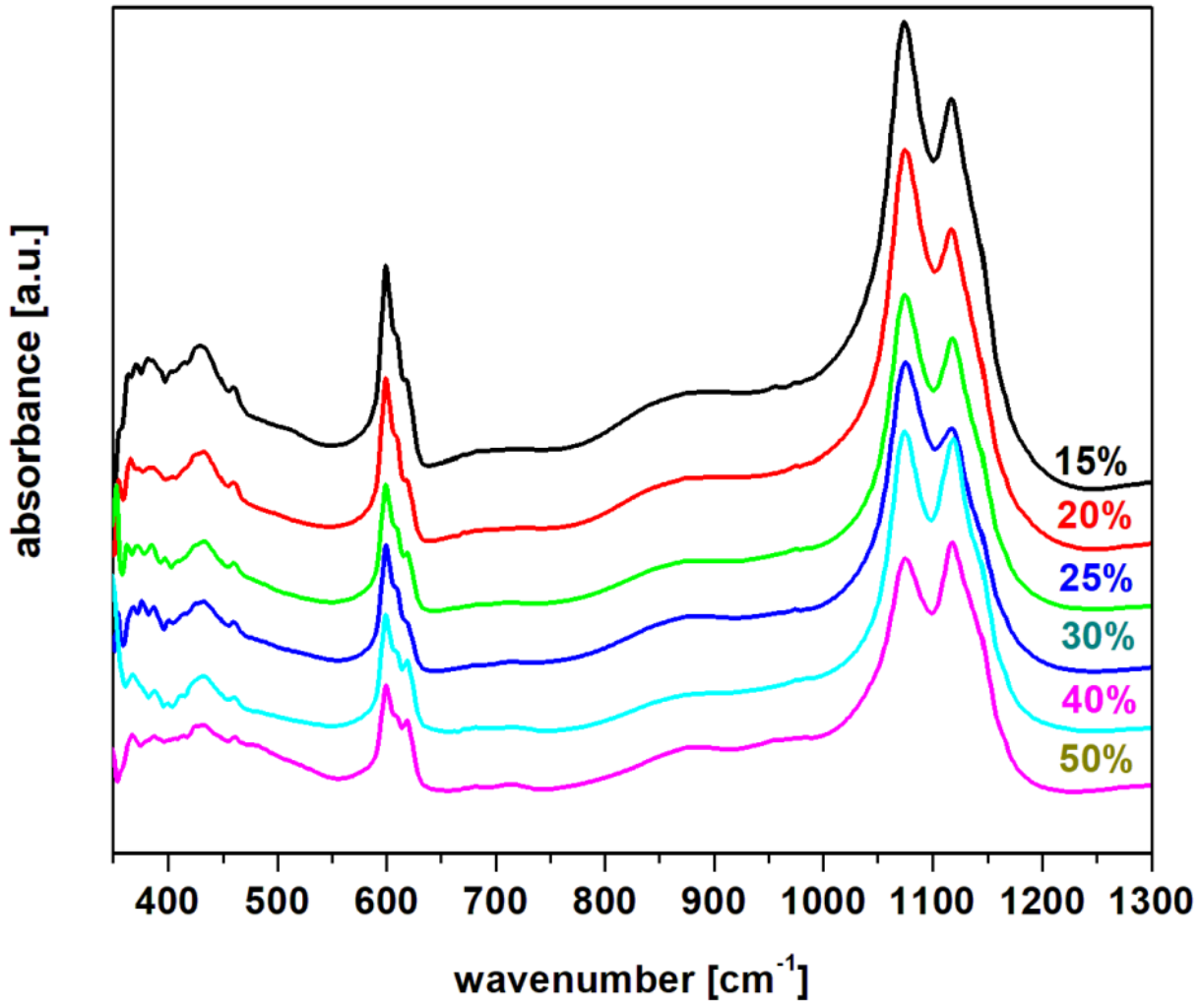

Figure 2b

Preprints (www.preprints.org) | NOT PEER-REVIEWED | Posted: 8 July 2022 doi:10.20944/preprints202207.0129.v1

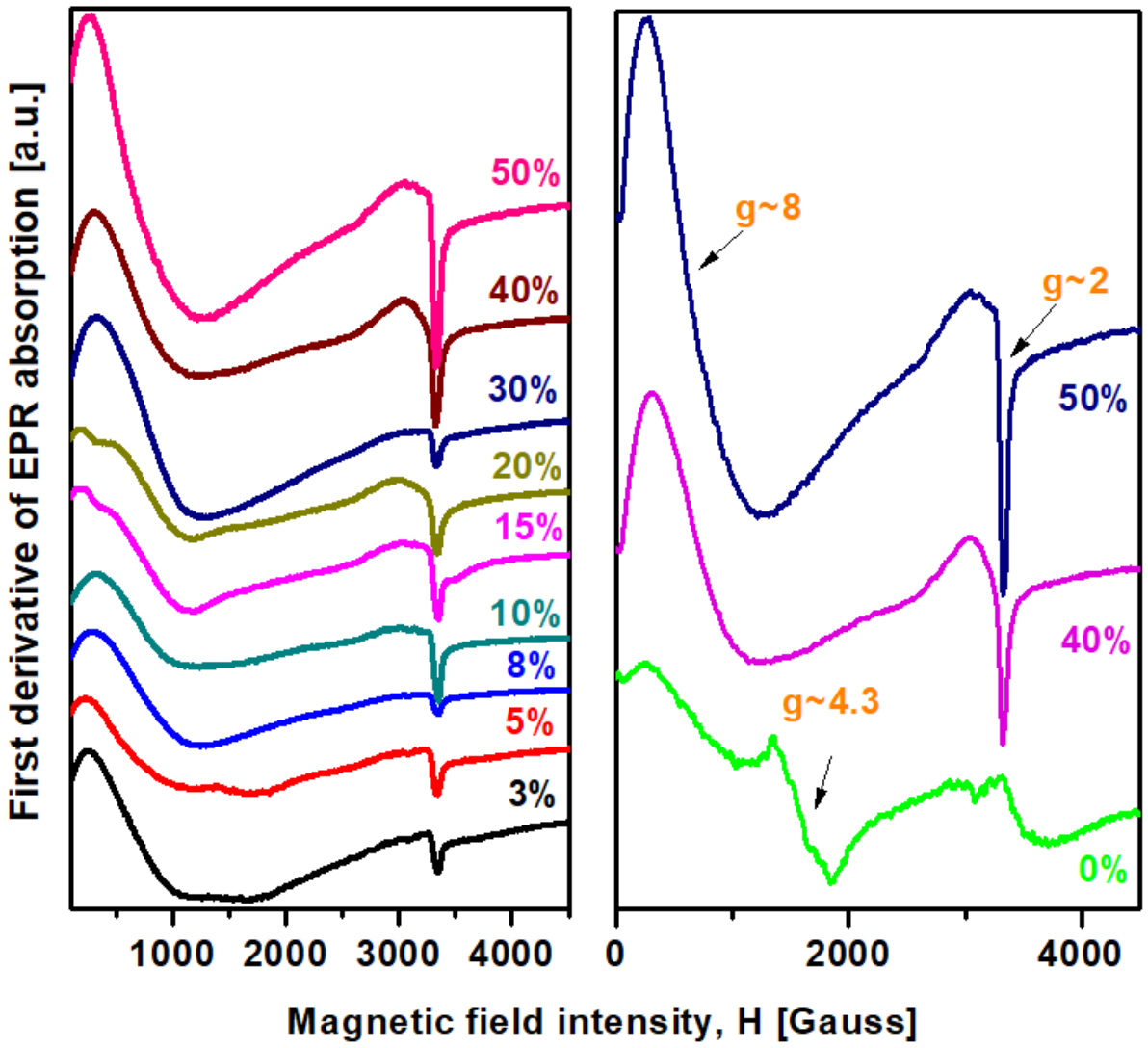

Figure 3

Preprints (www.preprints.org) | NOT PEER-REVIEWED | Posted: 8 July 2022 doi:10.20944/preprints202207.0129.v1

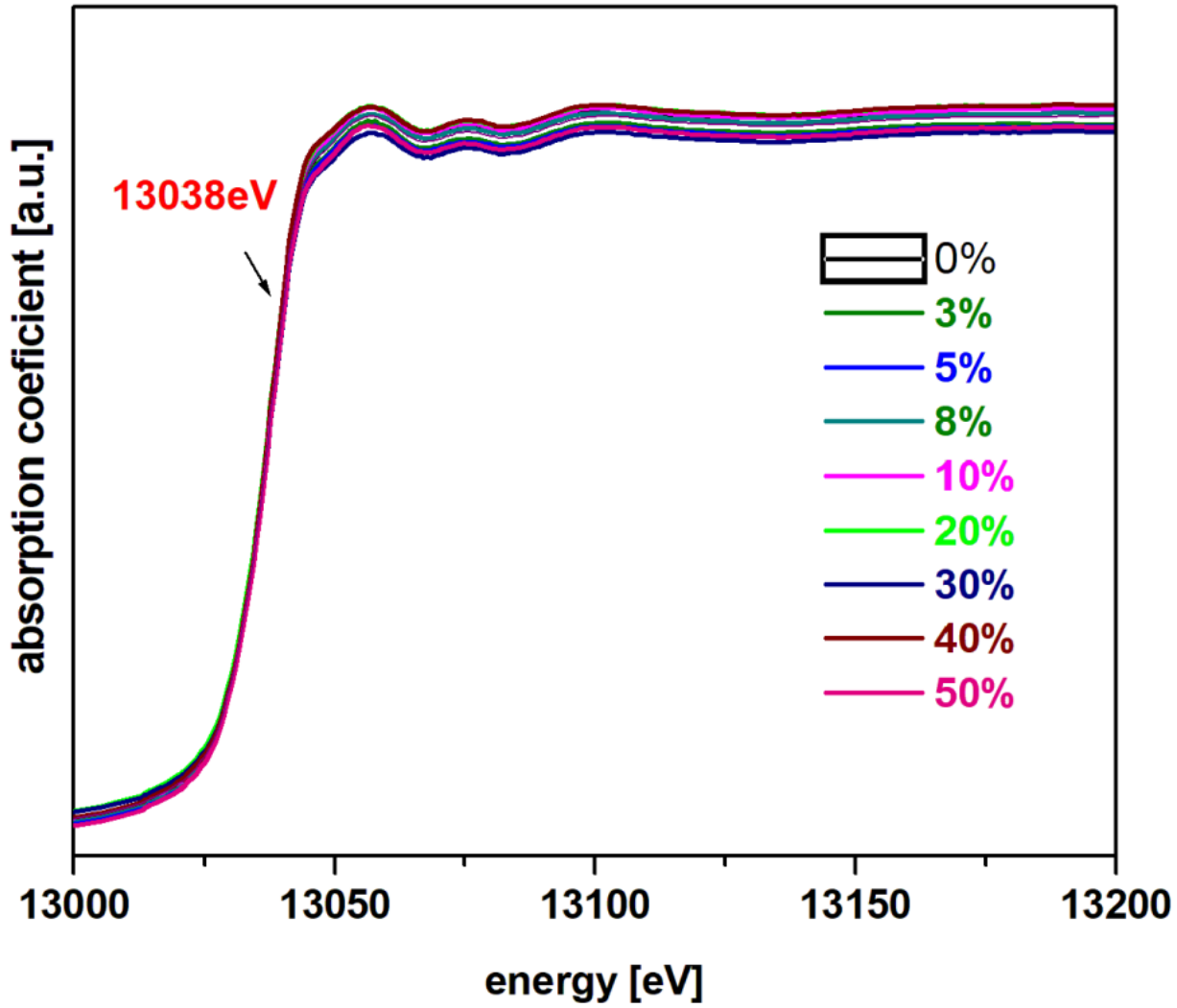

Figure 4

Preprints (www.preprints.org) | NOT PEER-REVIEWED | Posted: 8 July 2022 doi:10.20944/preprints202207.0129.v1

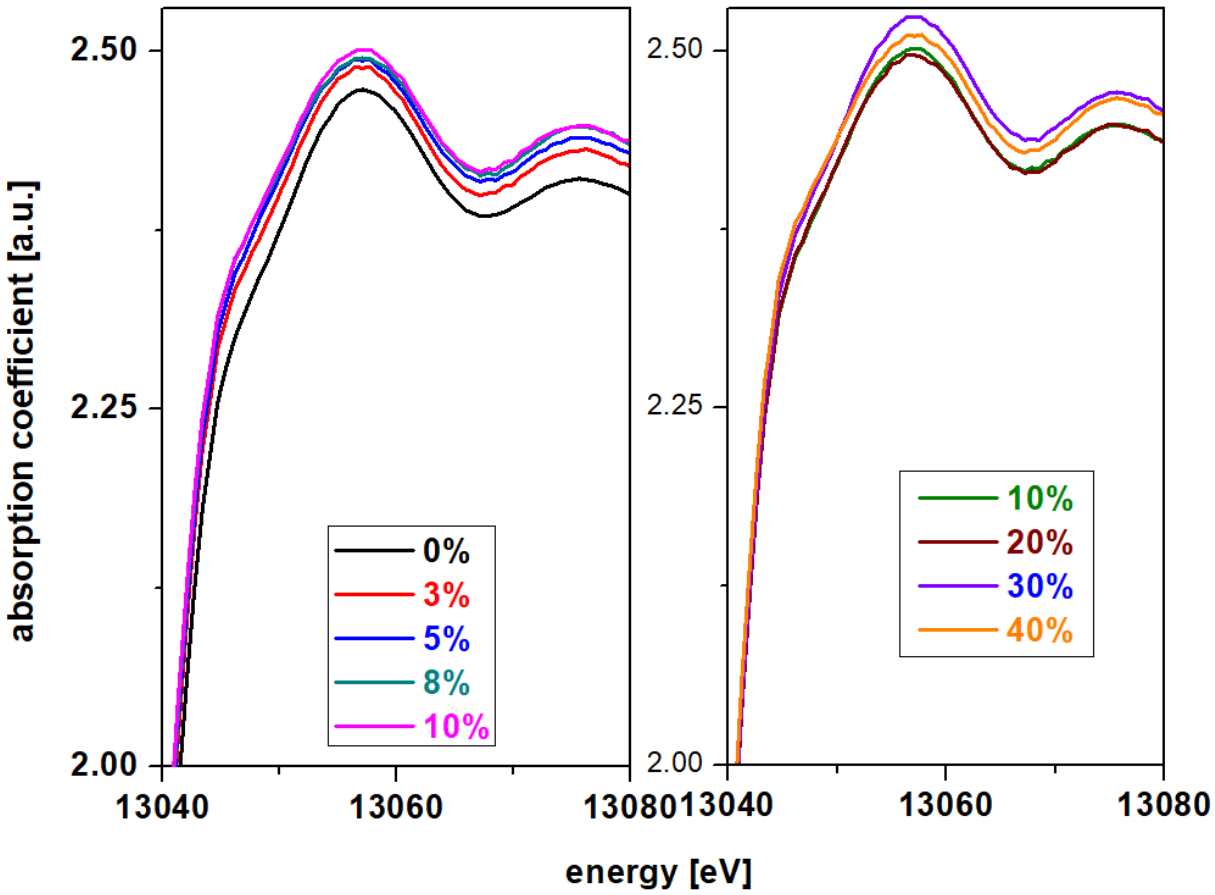

Figure 5

Preprints (www.preprints.org) | NOT PEER-REVIEWED | Posted: 8 July 2022 doi:10.20944/preprints202207.0129.v1

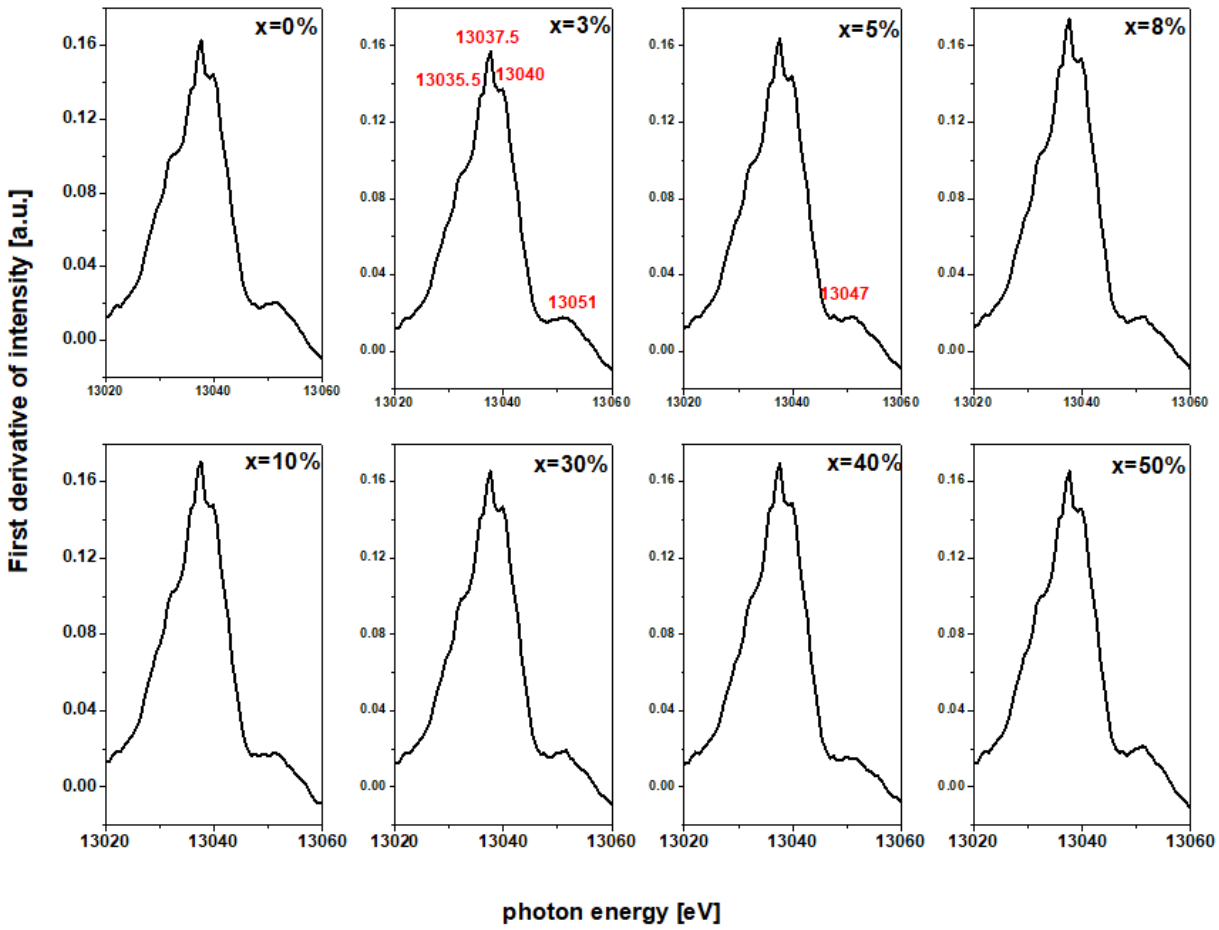

Figure 6

Preprints (www.preprints.org) | NOT PEER-REVIEWED | Posted: 8 July 2022 doi:10.20944/preprints202207.0129.v1

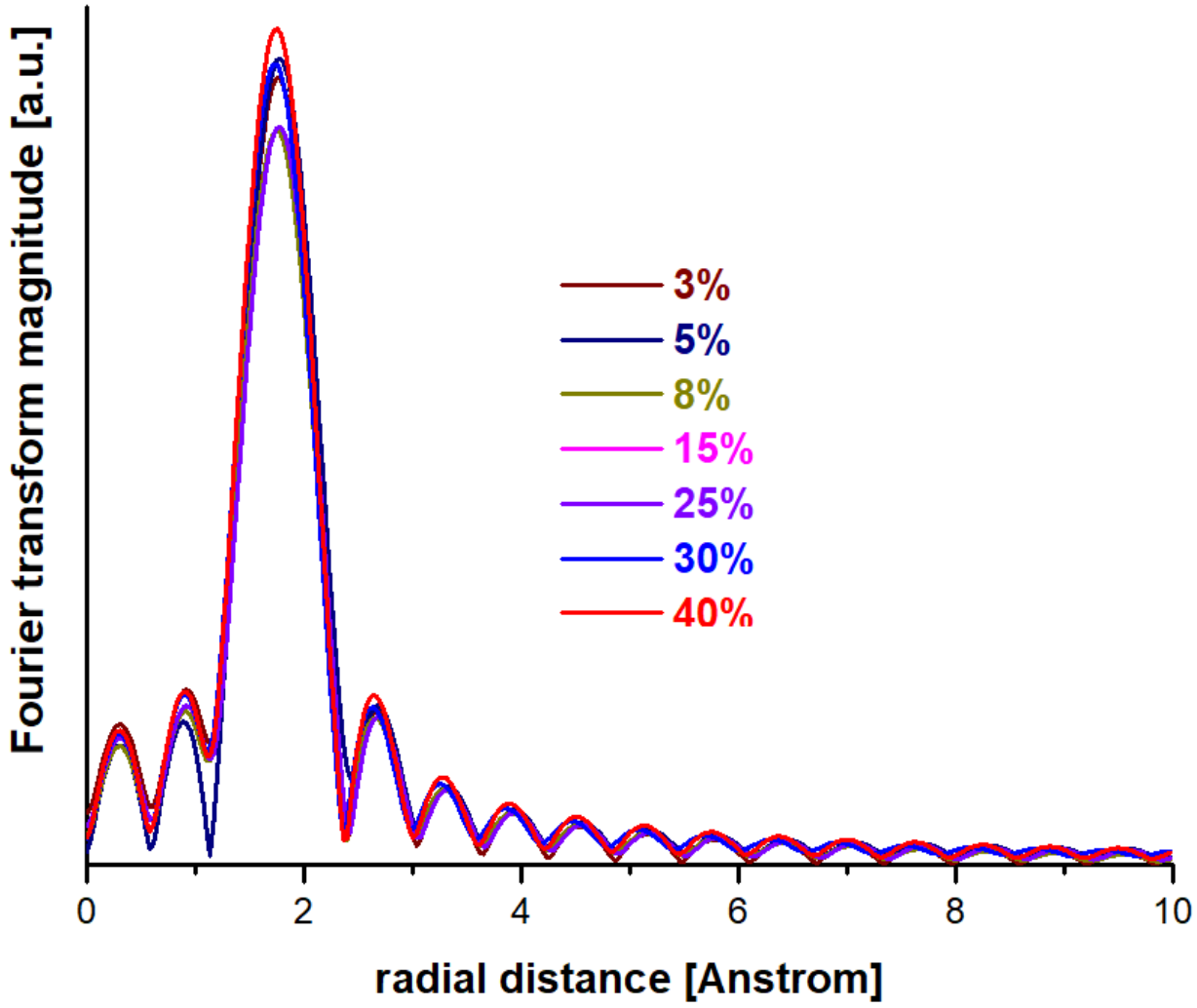

Figure 7

Preprints (www.preprints.org) | NOT PEER-REVIEWED | Posted: 8 July 2022 doi:10.20944/preprints202207.0129.v1

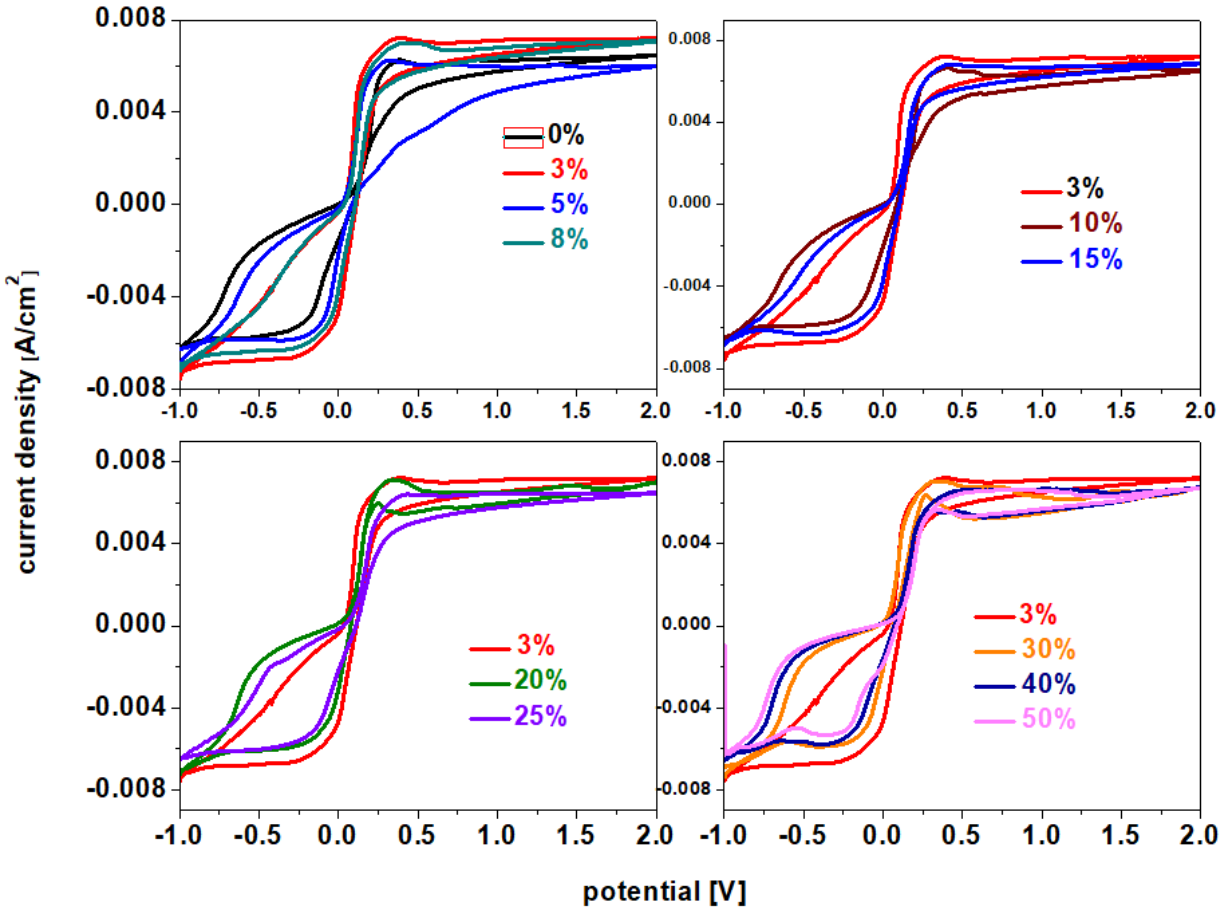

Figure 8

Preprints (www.preprints.org) | NOT PEER-REVIEWED | Posted: 8 July 2022 doi:10.20944/preprints202207.0129.v1

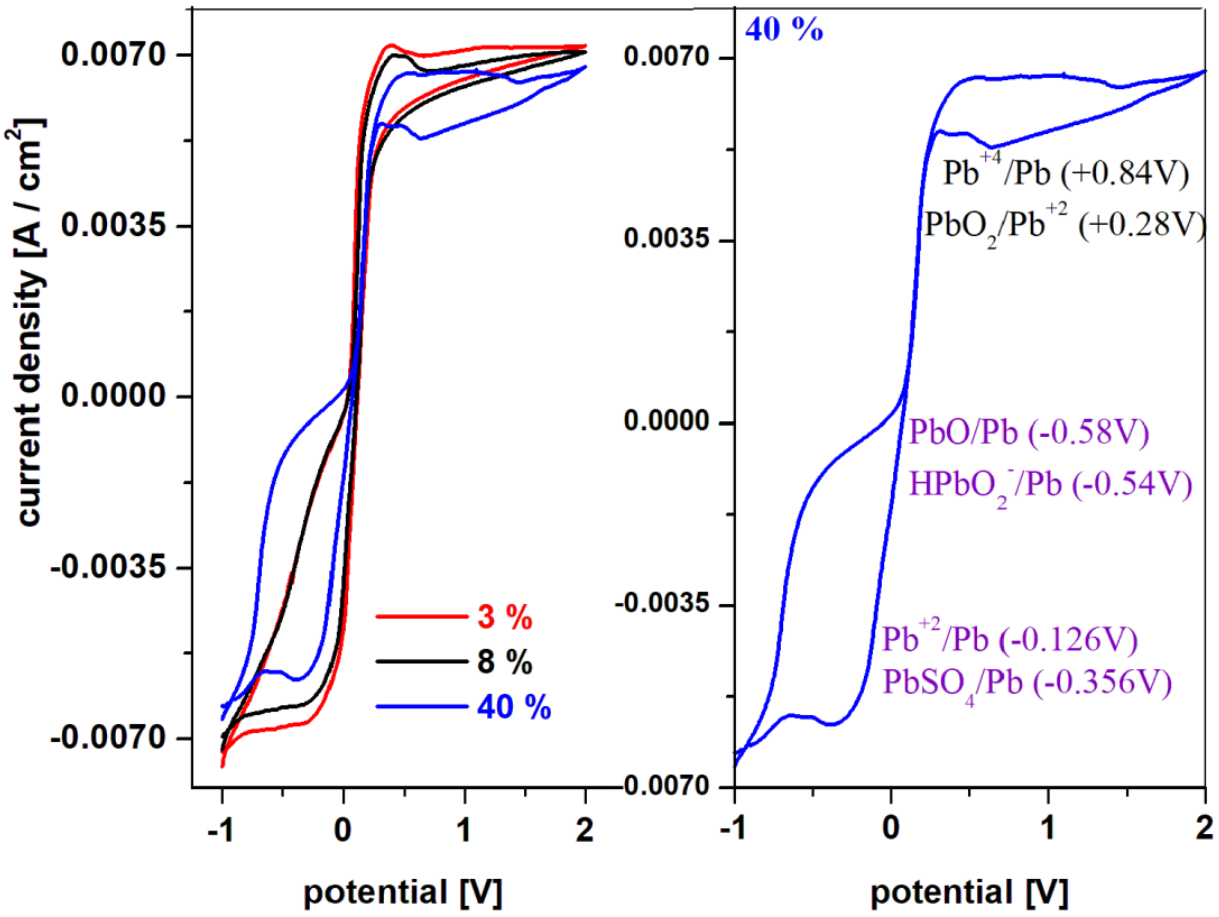

Figure 9

 doi:10.20944/preprints202207.0129.v1

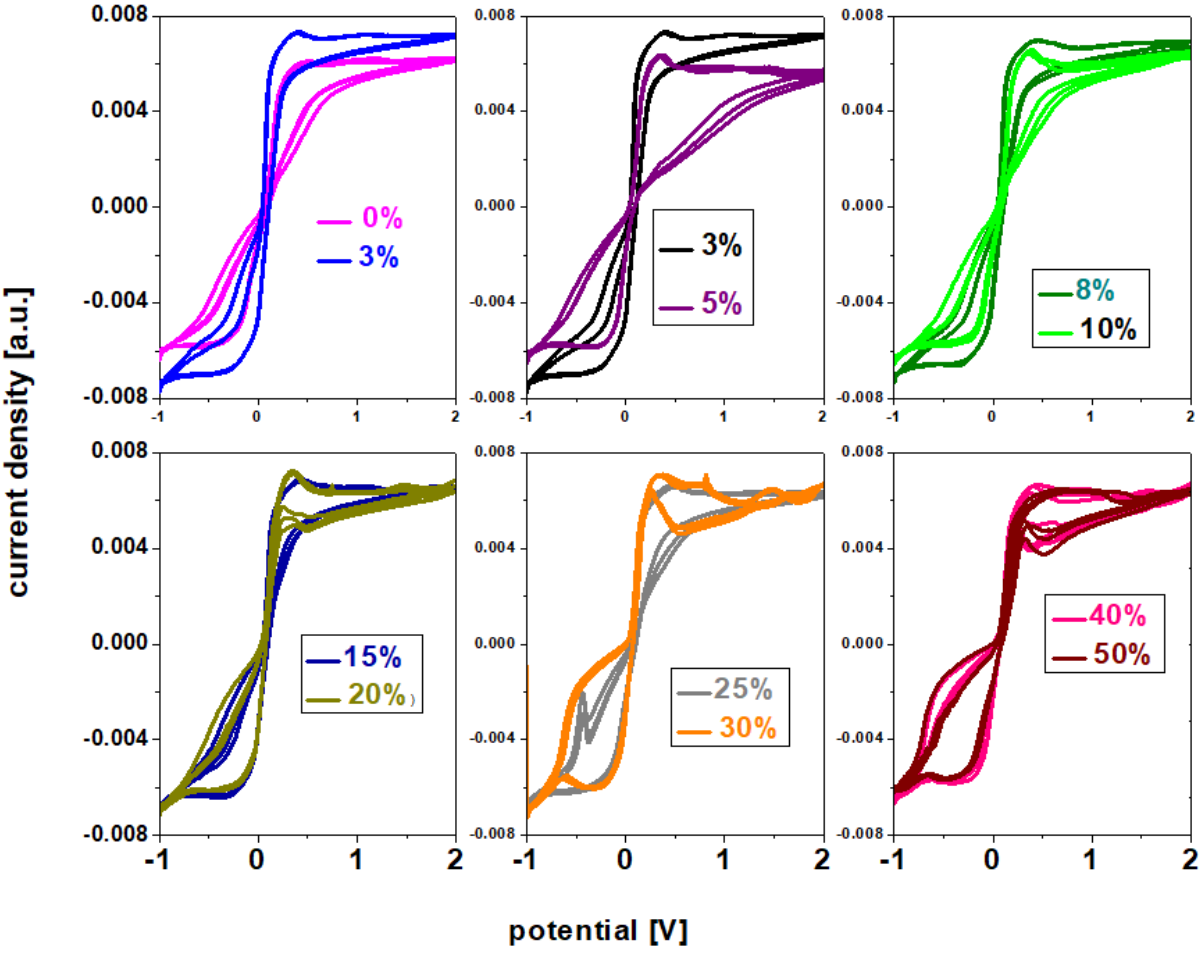

Figure 10